Acknowledgments. The authors wish to thank the technical staff of the Turku PET Centre for their efforts and skills dedicated to this project. Erja Mäntysalo is acknowledged for excellent assistance in animal PET imaging. The study was conducted within the Finnish Centre of Excellence in Molecular Imaging in Cardiovascular and Metabolic Research supported by the Academy of Finland, University of Turku, Turku University Hospital, and Åbo Akademi University. The study was further supported by grants from the Sigrid Juselius Foundation (N.K.), Turku University Hospital (EVO grants, A.A and A.R.), and from the Academy of Finland (grants no. 119048 and 218059, A.R). The study of N.K. was supported by grants from the Ministry of Education, Science, Sports and Culture, Grant-in-Aid for Young Scientists (start-up), 21890171, 2009–2010. A.A. is a Ph.D. student of Drug Discovery Graduate School.

Conflict of Interest Disclosure. The authors declare that they have no conflict of interest.

Appendix A

The image-based input function (C_A) was derived by a method previously developed for human cardiac study [10]. In that model, myocardial tissue radioactivity concentration (C_T) is described by the single-tissue compartment model as:

$$C_T(t) = fC_A(t) \otimes e^{-\frac{f}{p}t} \tag{1}$$

where f is MBF, p is myocardium to blood partition coefficient (P=0.9 1mL/g [10]) and $\otimes$ indicates the convolution integral. Radioactivity concentration in a selected LV ROI, LV(t), is described by:

$$\mathrm{LV}(t) = \beta C_A(t) + \gamma\rho C_T(t) \tag{2}$$

where β is recovery coefficient of LV, *i.e.*, it estimates PVE for C_A in LV ROI, ρ is myocardial tissue density (1.04 g/mL [10]), and γ is the spillover fraction of tissue radioactivity into LV ROI. The components of spillover of tissue radioactivity into the LV ROI (γ) is the residual of the recovery coefficient of the LV (β): $\gamma+\beta=1$. The measured radioactivity concentration in a selected Myo ROI, $R(t)$, is described by:

$$R(t) = \alpha f C_A(t) \otimes e^{-\frac{f}{p}t} + V_a C_A(t) \tag{3}$$

where α is tissue fraction, *i.e.*, it estimated PVE for Myo in Myo ROI, and V_a is arterial blood volume. The Eqs. 1 to 3 gives:

$$R(t) = \left(\frac{\alpha}{\beta} - \frac{(1-\beta)}{\beta^2}\rho V_a\right) f \cdot \mathrm{LV}(t) \otimes e^{-\left(\frac{1}{p}+\frac{(1-\beta)}{\beta}\rho\right)ft} + \frac{V_a}{\beta}\mathrm{LV}(t) \tag{4}$$

$$C_A(t) = \frac{1}{\beta}\mathrm{LV}(t) - \frac{(1-\beta)}{\beta^2} f \cdot \mathrm{LV}(t) \otimes e^{-\left(\frac{1}{p}+\frac{(1-\beta)}{\beta}\rho\right)ft} \tag{5}$$

The values of f, α, β, and V_a were estimated by nonlinear least squares regression analysis (Gauss–Newton algorithm) of $R(t)$ and LV(t) to Eq. 4. The true input function can be calculated from Eq. 5 using the calculated values of f, α, β, and V_a.

Appendix B

The measured blood curve was corrected for dispersion by using a model function. In the present experiment set-up, the transit time in the detector sensitive region was around 10 to 20 s, and this caused another type of dispersion than the previously developed method [18]; hence, the measured blood curve is expressed by convolving a rectangular function with width T_w (s) from a true input function.

To correct for the present type of dispersion, firstly, we determined T_w (s) by comparing measured blood radioactivity curve and image-based input function. For this purpose, we fitted the image-based input function using a model function for the input, and obtained the parameters of the model function. The model function (C_A) was derived by assuming the physiological and experimental conditions expressed as:

$$\begin{aligned}
C_A(t) &= 0. && (t < t_1)\\
&= A\left[\frac{1-\exp(\beta(t_1-t))}{\beta} + \frac{\alpha(1-\exp(\beta(t_1-t)))}{a(1-a)\beta} - \frac{\alpha(\exp(K_E(1-a)(t_1-t))-\exp(\beta(t_1-t)))}{a(1-a)\gamma}\right] && (t_1 \le t \le t_2)\\
&= A\left[\begin{array}{l}\frac{\exp(\beta(t_2-t))-\exp(\beta(t_1-t))}{\beta} + \frac{\alpha(\exp(\beta(t_2-t))-\exp(\beta(t_1-t)))}{a(1-a)\beta}\\ \quad + \frac{\alpha(\exp(K_E(1-a)(t_1-t_2)+\beta(t_2-t))-\exp(\beta(t_1-t)))}{a(1-a)\gamma}\\ \quad + \frac{\alpha(\exp(K_E(1-a)t_2)-\exp(K_E(1-a)t_1))(\exp(K_E(1-a)t)-\exp(\gamma t_2-\beta t)))}{a(1-a)\gamma}\end{array}\right] && (t > t_2)
\end{aligned} \tag{6}$$

$$\alpha = K_1/K_E,\quad \beta = K_E + K_1/a\quad \gamma = aK_E + K_1/a$$

$$a = (\alpha - 1 + K_C/K_E)/2 + \sqrt{\alpha + (\alpha - 1 + K_C/K_E)^2/4}$$

The derivation of this model function is described in detail in our previous papers [9, 29]. Briefly, the model function was created by assuming a three-compartment model in which (1) the tracer is administered in a rectangular form, (2) it diffuses bidirectionally between arterial (first compartment) and whole-body peripheral tissues (second compartment), and (3) the third compartment expresses a clearance of tracer in organs such as kidney. A is a scalar parameter reflecting the given amount of tracer, and t_1 and t_2–t_1 represent the appearance time of the tracer and the duration of administration, respectively. K_E (mL/min) and K_I (mL/min) represent the tracer bidirectional diffusion rates between arterial blood and whole-body interstitial spaces, respectively, and K_C (mL/min) represents the clearance rate of the tracer.

Second, a dispersed model function (C_M) was formulated by convolving with a rectangular function from the model function C_A as:

$$C_M(t - T_d) = C_A(t) \otimes R(t) \quad (7)$$

where $R(t)$ is the rectangular function with width T_w, and $\otimes$ indicates the convolution integral. Then, using the parameters obtained in the first step above in the same subject, the measured blood curve was fitted using Eq. 7, and T_w as well as delay time T_d were estimated. The mean of T_w was computed for eight blood curves as: T_w=19.5±1.4 s.

Third, the blood curve was fitted with the model function Eq. 7 again, fixing T_w as the obtained mean, and the parameters consisting Eq. 6 were estimated.

Finally, a corrected blood-based input function was obtained by applying the obtained parameters into the model function, Eq. 6.

References

1. Ploux L, Mastrippolito R (1998) *In vivo* radiolabel quantification in small-animal models. Nucl Med Biol 25:737–742
2. Myers R, Hume S, Bloomfield P et al (1999) Radio-imaging in small animals. J Psychopharmacol 13:352–357
3. Dupont P, Warwick J (2009) Kinetic modelling in small animal imaging with PET. Methods 48:98–103
4. Hoff J (2000) Methods of blood collection in the mouse. Lab Anim (NY) 29:47–53
5. Wu HM, Sui G, Lee CC et al (2007) *In vivo* quantitation of glucose metabolism in mice using small-animal PET and a microfluidic device. J Nucl Med 48:837–845
6. Weber B, Burger C, Biro P et al (2002) A femoral arteriovenous shunt facilitates arterial whole blood sampling in animals. Eur J Nucl Med Mol Imaging 29:319–323
7. Weber B, Späth N, Wyss M et al (2003) Quantitative cerebral blood flow measurements in the rat using a beta-probe and $H_2{}^{15}O$. J Cereb Blood Flow Metab 23:1455–1460
8. Fang YH, Muzic RF Jr (2008) Spillover and partial-volume correction for image-derived input functions for small-animal ^{18}F-FDG PET studies. J Nucl Med 49:606–614
9. Kudomi N, Bucci M, Oikonen V, et al (2011) Extraction of input function from rat [^{18}F]FDG PET images Mol Imaging Biol (in press)
10. Iida H, Rhodes CG, de Silva R et al (1992) Use of the left ventricular time-activity curve as a noninvasive input function in dynamic oxygen-15-water positron emission tomography. J Nucl Med 33:1669–1677
11. Strijckmans K, Vandecasteela C, Sambre J (1983) Production and quality control of [^{15}O]O_2 and [^{15}O]CO_2 for medical use. Int J Appl Radiat Isot 36:279–283
13. Sipilä HT, Clark JC, Peltola O et al (2001) An automatic [^{15}O]H_2O production system for heart and brain studies. J Labelled Compd Rad 44:S1066–S1068
14. de Jong HW, van Velden FH, Kloet RW et al (2007) Performance evaluation of the ECAT HRRT: an LSO-LYSO double layer high resolution, high sensitivity scanner. Phys Med Biol 52:1505–1526
15. Sipilä HT, Roivainen A, Kudomi N, et al A Multi-wire proportional counter for measurement of positron-emitting radionuclides during on-line blood sampling. In: Nuclear Science Symposium Conference Record, NSS'10. IEEE, Knoxville, TN
16. Iida H, Higano S, Tomura N et al (1988) Evaluation of regional differences of tracer appearance time in cerebral tissues using [^{15}O] water and dynamic positron emission tomography. J Cereb Blood Flow Metab 8:285–288
17. Yee SH, Jerabek PA, Fox PT (2005) Non-invasive quantification of cerebral blood flow for rats by microPET imaging of 15O labelled water: the application of a cardiac time-activity curve for the tracer arterial input function. Nucl Med Commun 26:903–911
18. Iida H, Kanno I, Miura S et al (1986) Error analysis of a quantitative cerebral blood flow measurement using $H_2{}^{15}O$ autoradiography and positron emission tomography, with respect to the dispersion of the input function. J Cereb Blood Flow Metab 6:536–545
19. Munk OL, Keiding S, Bass L (2008) A method to estimate dispersion in sampling catheters and to calculate dispersion-free blood time-activity curves. Med Phys 35:3471–3481
20. Pain F, Lanièce P, Mastrippolito R et al (2004) Arterial input function measurement without blood sampling using a beta-microprobe in rats. J Nucl Med 45:1577–1582
21. Laforest R, Sharp TL, Engelbach JA et al (2005) Measurement of input functions in rodents: challenges and solutions. Nucl Med Biol 32:679–685
22. Croteau E, Bénard F, Bentourkia M et al (2004) Quantitative myocardial perfusion and coronary reserve in rats with ^{13}N-ammonia and small animal PET: impact of anesthesia and pharmacologic stress agents. J Nucl Med 45:1924–1930
23. Huang SC, Barrio JR, Yu DC et al (1991) Modelling approach for separating blood timeactivity curves in positron emission tomographic studies. Phys Med Biol 36:749–761
24. Iida H, Jones T, Miura S (1993) Modeling approach to eliminate the need to separate arterial plasma in oxygen-15 inhalation positron emission tomography. J Nucl Med 34:1333–1340
25. Kudomi N, Hayashi T, Watabe H et al (2009) A physiologic model for recirculation water correction in CMRO2 assessment with $^{15}O_2$ nhalation PET. J Cereb Blood Flow Metab 29:355–364
26. Nakao Y, Itoh Y, Kuang TY et al (2001) Effects of anesthesia on functional activation of cerebral blood flow and metabolism. Proc Natl Acad Sci USA 98:7593–7598
27. Moskalenko YuE, Rovainen C, Woolsey TA et al (1995) Combinations of methods for monitoring the microcirculation of the brain. Neurosci Behav Physiol 25:266–272
28. Pain F, Laniece P, Mastrippolito R et al (2000) SIC, an intracerebral radiosensitive probe for *in vivo* neuropharmacology investigations in small laboratory animals: theoretical considerations and physical characteristics. IEEE Trans Nucl Sci 47:25–32
29. Kudomi N, Järvisalo MJ, Kiss J et al (2009) Non-invasive estimation of hepatic glucose uptake from [^{18}F]FDG PET images using tissue-derived input functions. Eur J Nucl Med Mol Imaging 36:2014–2026

専門医に求められる
最新の知識 脳血管障害
脳神経外科速報 vol.22 no.2 180～187, 2012

もやもや病と過灌流現象 — 過灌流における脳循環動態

賀来泰之[1, *)]，飯原弘二[1)]
Yasuyuki KAKU, Koji IIHARA
1）国立循環器病研究センター脳神経外科　〒565-8565　大阪府吹田市藤白台5-7-1
＊現籍：熊本大学脳神経外科　〒860-8556　熊本市本荘1-1-1

もやもや病に対する血行再建術後の局所過灌流が最近注目されているが，その病態，特に過灌流時の脳循環動態については不明な点が多い．今回，術後急性期に^{15}O-gas PETを施行し脳循環代謝の評価を行ったので，結果について報告するとともに過灌流の病態について考察する．

Key Words: もやもや病，過灌流，脳循環代謝，PET

Ⅰ．はじめに

もやもや病は頭蓋内の主要動脈の狭窄と側副血行路の発達を特徴とする疾患であり，脳虚血症状や出血性合併症を生じることが知られている[1)]．虚血症状を呈する例に対しては浅側頭動脈（STA）－中大脳動脈（MCA）吻合術などの直接バイパスや種々の間接バイパスが有効な治療として確立している[2, 3)]．良好な治療成績が報告されている一方で，直接バイパス術後急性期にはバイパス吻合部周囲の局所的高灌流が一過性の神経症状や痙攣，頭痛などの原因となっており，術後の過灌流現象として注目されている[4-10)]．血行再建術後の過灌流は頚動脈内膜剥離術（CEA）後の合併症として認知されており，その病態は脳組織のデマンドに対しての過剰な脳血流の増加と考えられている[11, 12)]．脳循環動態の評価は正確にはPET検査によって行われるべきだが，最近では^{123}I-IMP-ARG法[13)]などのような簡便で精度の高い脳血流SPECT定量画像が臨床応用され代用されていることが多い．過灌流の評価も脳血流SPECTで行われるのが一般的で，過灌流時の脳循環代謝についての詳細な報告はない．本研究では，STA-MCAバイパス術後の過灌流症候群について^{15}O-gas PETを用いて評価を行った．

Ⅱ．対象・方法（図1）

対象は2009年4月から2011年7月の期間に国立循環器病研究センターで治療を行った成人もやもや病34例（15～70歳：平均39.3歳）42半球である．小児例は除外した．全症例に対してSTA-MCAバイパス術を行い，術中は脳血流dopplerおよびindocyanine green（ICG）video-angiographyを用いてバイパスの開存を確認した

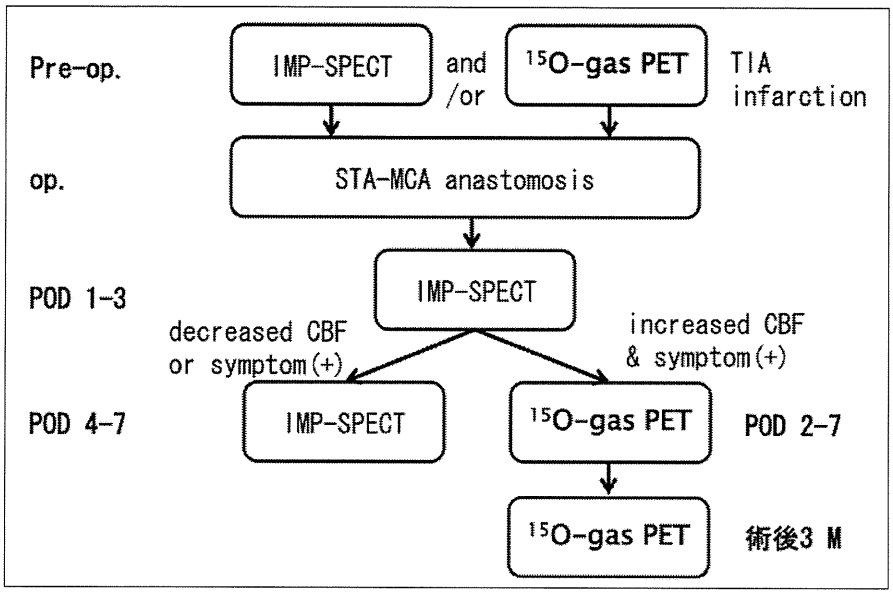

図1　脳血流検査のプロトコール

(図2). 術前に ^{123}I-IMP SPECT もしくは ^{15}O-gas PET を行い脳循環動態の評価を行った. 特に, 術前に虚血症状が強い20例23半球に対しては積極的に ^{15}O-gas PET を施行した. 術後は全例で術後1～3日以内に ^{123}I-IMP SPECT を施行し, 術前に比べ脳血流の増加かつ神経症状を呈する例では症候性過灌流と判断し術後急性期に ^{15}O-gas PET を施行, また術後3カ月目にも ^{15}O-gas PET を施行した (図1). 術前, 術後2～7日, 術後3カ月での PET パラメータの評価を行った.

Ⅲ. 過灌流症候群の定義

STA-MCA バイパス術後の局所過灌流についての明確な定義はない. そこで, 症候性の過灌流を術後の ^{15}O-gas PET での脳血流定量値が正常値 + 2SD (57.8 mL/100 g/min) 以上で, バイパス吻合部位周囲の局所的高灌流が原因と考えられる一過性の局所神経脱落症状や強い頭痛, 痙攣を呈するものと定義した.

Ⅳ. 結　果

術前の血行力学的脳虚血ステージを PET[14] もしくは SPECT[30] で評価を行ったところ, stage Ⅰ相当が18半球, stage Ⅱ相当が24半球であった. 症候性過灌流は5例6半球 (6/42, 14.3%) に認めた. 症例と経過の一覧を表1に示す. 術後に症候性過灌流を呈した5例はいずれも虚血発作での発症であり, 術前の血行力学的ステージは stage Ⅰ相当が1半球 (1/18, 5.9%), stage Ⅱ相当が5半球 (5/24, 20.8%) で, stage Ⅱでは高率に術後過灌流を呈した. 過灌流を呈した部位は STA-MCA バイパス吻合部周囲で, 症状は痙攣,

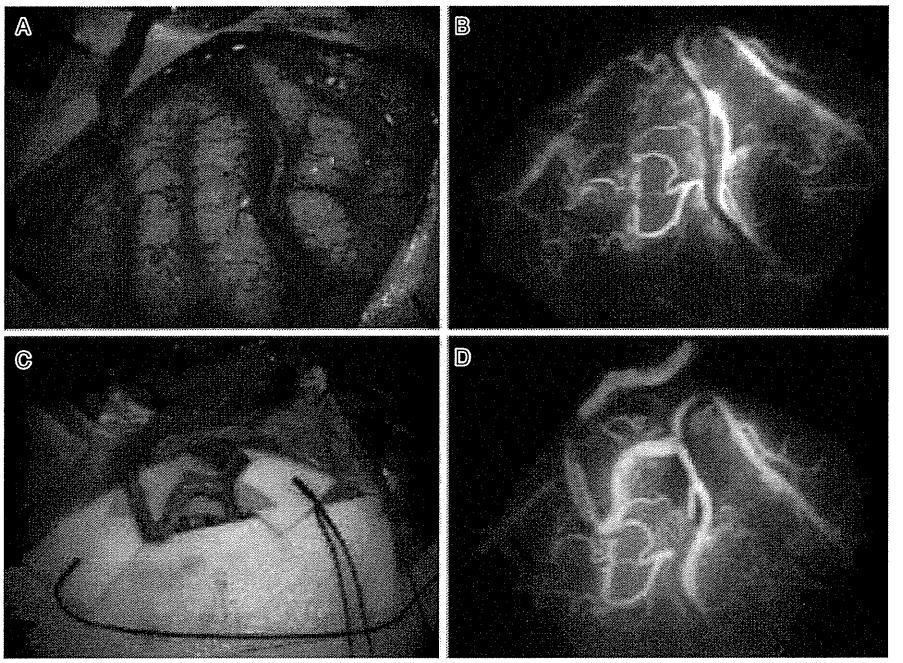

図2　症例 no. 5 の術中画像，左 STA-MCA バイパス
A：吻合前．脳表には拡張した細動脈を多数認める．
B：吻合前の ICG videoangiography．動脈相での脳表の濃染が疎である．
C：STA parietal branch と M4 の吻合を施行．
D：吻合後の ICG videoangiography．バイパスからの血流により動脈相での脳表の濃染像が改善している．ただし，この時点で術後の過灌流を予測することは困難である．

感覚障害，失語症状がそれぞれ 2 例ずつであった．過灌流の症状は術後 1 ～ 4 日目の早期に出現し，持続期間は 4 ～ 14 日であった．術後 3 カ月での mRS はいずれも良好であった．

V．PET 定量値

表 2 に示す．脳血流量 CBF は術前 37.6 ± 5.1 mL/100 g/min（n = 4）に比べ過灌流 77.6 ± 10.7 mL/100 g/min（n = 6）では有意に増加を認めた．脳血液量 CBV は術前 5.83 ± 1.88 mL/100 g，過灌流 6.80 ± 1.46 mL/100 g と術前からの高値が持続していた．脳酸素代謝量 $CMRO_2$ は術前 3.70 ± 0.31 mL/100 g/min で，過灌流では 4.42 ± 0.88 mL/100 g/min と増加を認めた．術後過灌流を呈した 6 例中 4 例の $CMRO_2$（3.83 ± 0.33 mL/100 g/min）は正常域で推移したが，痙攣を呈した 2 例では $CMRO_2$（5.60 ± 0.10 mL/100 g/min）の著明な上昇を認めた．CBF の著明な上昇と $CMRO_2$ の軽度上昇の結果，酸素摂取率 OEF は術前 0.58 ± 0.05 の高値から過灌流では

表1　過灌流症候群をきたした5例6半球の臨床像

症例 no.	年齢，性別	発症形式	術前の血行力学的ステージ	左右	術後過灌流の範囲	症候	過灌流の発症時期	持続期間（days）	mRS score 術後 3M
1	37，M	TIA	stage Ⅰ*	R	central & parietal	痙攣	POD 4	4	0
2	44，F	梗塞	stage Ⅱ	L	central	痙攣	POD 3	7	1
3	44，F	梗塞	stage Ⅱ	R	central	感覚障害	POD 3	11	1
4	41，F	TIA	stage Ⅱ	R	central	感覚障害	POD 3	7	0
5	60，F	梗塞	stage Ⅱ	L	pre- & central	失語	POD 1	11	0
6	51，M	TIA	stage Ⅱ*	L	pre-，central & parietal	失語	POD 3	14	0

POD = post-operative day，pre- = precentral，mRS = modified Rankin Scale
症例2と3は同一患者，* IMP-SPECT での脳血流評価.

表2　PET パラメータの推移

	pre op.（n = 4）	hyper-（n = 6）	post op.（n = 6）	P value hyper- vs. pre op.	P value hyper- vs. post op.
CBF（mL/100 g/min）	37.5 ± 5.1	77.6 ± 10.7*	44.2 ± 4.2	<0.01	<0.01
CBV（mL/100 g）	5.83 ± 1.87*	6.80 ± 1.46*	4.27 ± 0.40*	n.s.	0.021
$CMRO_2$（mL/100 g/min）	3.70 ± 0.31	4.42 ± 0.89	3.58 ± 0.44	n.s.	0.034
OEF	0.58 ± 0.05*	0.40 ± 0.08	0.48 ± 0.04	<0.01	0.024
CBF/CBV（min^{-1}）	7.37 ± 1.93	12.5 ± 4.09	12.0 ± 2.45	n.s.	n.s.

* Values out of the mean ± 2SD range of controls
hyper- = hyperperfusion，n.s. = not significant
3群間の検定には ANOVA にて $p<0.01$，各群間についての有意差検定は Scheffe 検定にて行った.

0.40 ± 0.08 と有意に低下した．脳灌流圧 CPP の指標である CBF/CBV は術前 7.4 ± 1.9 min^{-1} と低値であったが，過灌流では 12.5 ± 4.1 min^{-1} と増加を認めた．術後3カ月では，CBF，$CMRO_2$，OEF は正常域となり，CBV，CBF/CBV は術前に比べ改善した．

Ⅵ．代表例

41歳，女性（症例 no. 4）．5年前から左半身の脱力発作を自覚していたが，最近になりその頻度

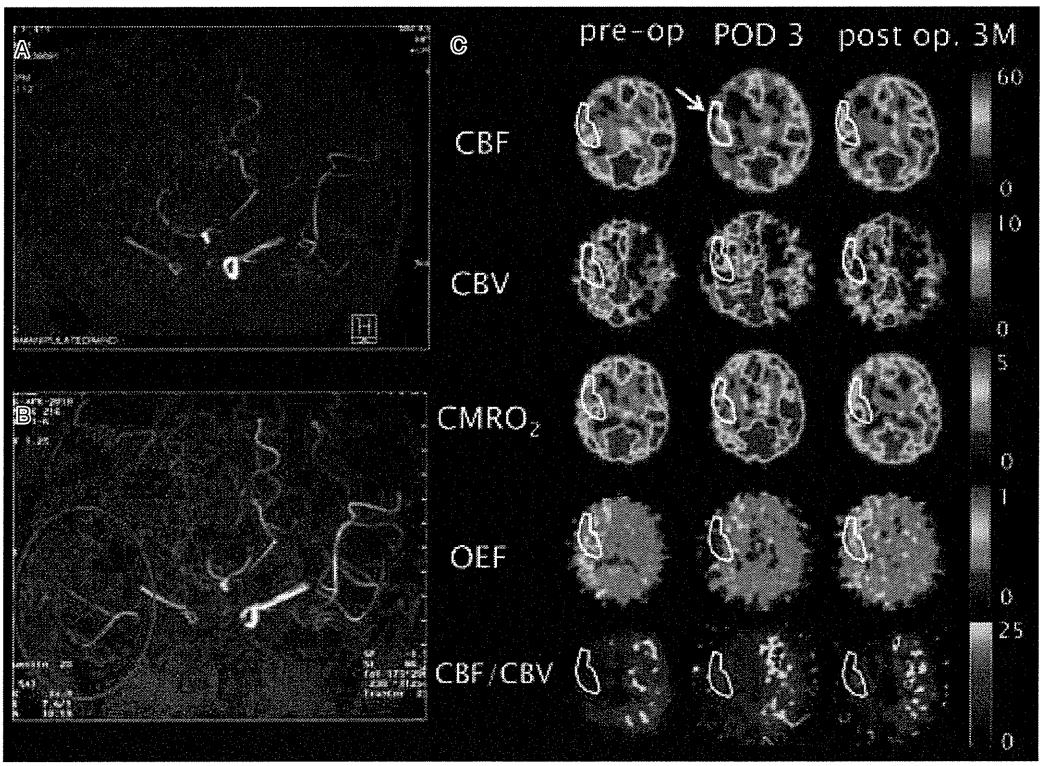

図 3　症例 no. 4

A：術前 MRA，B：術後 MRA．バイパスの patency は良好である．
C：PET パラメータの推移．左側：術前は右半球で著明な CBF の低下を認め，CBV は上昇，$CMRO_2$ は正常であるが，OEF は上昇し，いわゆる misery perfusion の状態である．脳灌流圧の指標となる CBF/CBV は対側に比べ著明に低下している．中央：術後 3 日目（POD 3）では CBF は著明に増加し（矢印），CBV の高値は持続，$CMRO_2$ はわずかに増加，OEF は低下している．右側：術後 3 カ月では，CBF，$CMRO_2$，OEF は正常となり，CBV と CBF/CBF は術前に比べ改善を認める．

が増えたため精査を行った．頭部 MRI/A，脳血管撮影でもやもや病の確定診断となった．^{15}O-gas PET では右半球の貧困灌流を認めた（**図 3**）．右半球に対して STA-MCA バイパス術を施行した．術後 2 日目までは特に症状なく経過していたが，術後 3 日目より左半身のしびれ感を自覚，30 分程度のものが 1 日に数回出現した．術後 3 日目の PET ではバイパス吻合部周囲に著明な CBF の増加を認め，過灌流症候群の診断で厳重な血圧管理を行った．術後 7 日目まで症状は続いたが自然に消失し，術後 10 日目には独歩退院となった．

Ⅶ. 考　察

1）過灌流症候群

もやもや病に対する血行再建術後の俗にいう過灌流症候群は，これまでの成人例での報告では自験例を含めて 14.3 ～ 21.5％に認めた[4, 8]．最近では，脳血流定性 SPECT での術後評価で無症候性

過灌流の存在も言われており，潜在的には高い頻度で過灌流を呈するものと推測する．症候性の過灌流について，CEA 術後の過灌流症候群の古典的 3 徴は頭痛，痙攣，脳出血であるが[11, 12, 15]，STA-MCA バイパス術後の一過性の神経脱落症状を過灌流症候群に含めてよいものであろうか．周術期には虚血性合併症も起こりえるが[7, 16]，今回の神経脱落症状（感覚障害，失語など）は局所の脳血流増加部位に起因するものと判断し，これらを過灌流症候群と定義した．

2）もやもや病における過灌流のメカニズム

術後過灌流では CBF は著明に増加するが，CEA/carotid artery stenting（CAS）術後の過灌流は術前の 100％（定量値で術前値の 2 倍）以上の増加とする[11, 12]のが一般的である．自験例では術前に比べ CBF は一過性に 53 ～ 120％（平均 106％）増加したが，100％未満の CBF の増加であっても症候性過灌流が起こり得ると言える．CBV 値の上昇は細動脈の拡張と関係があり[17, 18]，血管狭窄に伴う CBV 上昇は脳灌流圧の低下を引き起こす．自験例では術前の CBV 値は高値であり，過灌流でも CBV 高値は持続していた．術後 3 カ月の時点では術前に比べ CBV 値の低下を認めた．CEA/CAS 後の過灌流で報告されているように[19, 20]，術後急性期に CBV 値の回復の遅延はもやもや病においても術後過灌流の重要なメカニズムであると考えられる．過灌流の状態では CBF が上昇し脳灌流圧が上昇しているにもかかわらず CBV が低下しないのは，細動脈が術後早期には収縮しないためと考えられる．すなわち，自動調節能の障害による vasopararesis の状態が続いており，過灌流に伴う臨床症状は術後 1 日目から 14 日目まで継続したが，その間は vasopararesis が持続するものと推測される．それゆえ，過灌流時には血圧の上昇が脳血流の増加を助長するため厳重な血圧管理が必要となる[6]．また，TIA や脳梗塞など虚血発作で発症するもやもや病では CBV 値は著明に高値であり[21]，術前の CBV 高値は術後過灌流の予測因子と推測される．

脳灌流圧 CPP は一般的に脳血管予備能 CVR を反映し，CVR 低下例は CEA 術後の症候性過灌流の予測因子である[19, 22]．本研究において術前の CPP（CBF/CBV）は低値であり，術後急性期には増加を認めた．CPP は CBV 値と強く相関しており，術前 CPP の高度低下は術後過灌流のリスクファクターと考えられる．

過灌流時には $CMRO_2$ は増加し OEF は有意に低下した．しかし，67％（4/6 例）は過灌流時に $CMRO_2$ は正常域であったが，痙攣を呈した 2 例では $CMRO_2$ は著明に高値であった．痙攣発作は脳酸素代謝量の過剰な上昇をきたす異常な生理的状態であり[23]，痙攣発作中は $CMRO_2$ の増加に応じて CBF は増加する[24-27]．注意すべくは，術後過灌流を呈した例には痙攣発作のために 2 次的に脳血流が増加した例も存在する可能性があることである．脳血流 SPECT での測定だけでは過灌流が痙攣発作によるものなのどうかの判断は困難である．

Marchal ら[28]は脳梗塞後の再灌流障害・過灌流（postischemic hyperperfusion）について PET を用いた脳循環動態の評価を行い，患側では健側に比べ CBF，CBV，$CMRO_2$ の増加，OEF の低下を認め，総合的に hypermetabolic state である

と結論付けている．Postischemic hyperperfusionとSTA-MCAバイパス術後の局所過灌流を単純には比較できないが，本研究では術後痙攣発作を呈さなかった例では$CMRO_2$は過灌流でわずかに増加したが正常域で経過した．$CMRO_2$はCBFの増加に対して対数関数的に増加する[29]ため，過灌流では必ずしもCBFと$CMRO_2$がミスマッチの状態ではないと考えられる．また，過灌流の脳循環動態は脳組織のデマンドに対しての過剰な脳血流の増加[11, 12]と考えられてきたが，本研究の結果からは必ずしもそうではないようである．もやもや病に対する血行再建術後の過灌流現象については，脳循環代謝の解析では評価できないその他の因子も関与していると考えられ，さらなる研究が必要と思われる．

Ⅷ．まとめ

過灌流は，血行再建術後の急激な血流再開により自動調節能が障害された脳血管がただちに反応できず一時的な血流増加をきたすことと考えられてきたが，今回のPETでの脳循環動態の検討からはおそらくこれは正しいと考えられる．痙攣発作を除く症候性の過灌流の脳循環動態は，脳血流の著明な増加，脳血液量の高値持続および脳酸素代謝量の正常域での推移であり，結果として酸素摂取率は著明に低下する．

参考文献

1) Suzuki J, Takaku A: Cerebrovascular "moyamoya" disease: Disease showing abnormal net-like vessels in base of brain. Arch Neurol 20: 288-99, 1996
2) Kuroda S, Houkin K: Moyamoya disease: Current concepts and future perspectives. Lancet Neurol 7: 1056-66, 2008
3) Takahashi JC, Miyamoto S: Moyamoya disease: Recent progress and outlook. Neurol Med Chir (Tokyo) 50: 824-32, 2010
4) Fujimura M, Kaneta T, Mugikura S, et al: Temporary neurologic deterioration due to cerebral hyperperfusion after superficial temporal artery-middle cerebral artery anastomosis in patients with adult-onset moyamoya disease. Surg Neurol 67: 273-82, 2007
5) Fujimura M, Mugikura S, Kaneta T, et al: Incidence and risk factors for symptomatic cerebral hyperperfusion after superficial temporal artery-middle cerebral artery anastomosis in patients with moyamoya disease. Surg Neurol: 442-7, 2009
6) Fujimura M, Shimizu H, Inoue T, et al: Significance of focal cerebral hyperperfusion as a cause of transient neurologic deterioration after extracranial-intracranial bypass for moyamoya disease: Comparative study with non-moyamoya patients using n-isopropyl-p-[(123)i] iodoamphetamine single-photon emission computed tomography. Neurosurgery 68: 957-64, 2011; discussion 964-55
7) Hayashi T, Shirane R, Fujimura M, et al: Postoperative neurological deterioration in pediatric moyamoya disease: Watershed shift and hyperperfusion. J Neurosurg Pediatr 6: 73-81, 2010
8) Kim JE, Oh CW, Kwon OK, et al: Transient hyperperfusion after superficial temporal artery/middle cerebral artery bypass surgery as a possible cause of postoperative transient neurological deterioration. Cerebrovasc Dis 25: 580-6, 2008
9) Furuya K, Kawahara N, Morita A, et al: Focal hyperperfusion after superficial temporal artery-middle cerebral artery anastomosis in a patient with moyamoya disease. J Neurosurg 100: 128-32, 2004
10) Ogasawara K, Komoribayashi N, Kobayashi M, et al: Neural damage caused by cerebral hyperperfusion after arterial bypass surgery in a patient with moyamoya disease: Neurosurgery 56: E1380, 2005
11) Piepgras DG, Morgan MK, Sundt TM, Jr., et al: Intracerebral hemorrhage after carotid endarterectomy. J Neurosurg 68: 532-6, 1988
12) Sundt TM, Jr., Sharbrough FW, Piepgras DG, et al: Correlation of cerebral blood flow and electroencephalographic changes during carotid endarterectomy: With results of surgery and hemodynamics of cerebral ischemia. Mayo Clin Proc 56: 533-43, 1981

13) Iida H, Itoh H, Nakazawa M, et al: Quantitative mapping of regional cerebral blood flow using iodine-123-imp and spect. J Nucl Med 35: 2019-30, 1994
14) Powers WJ: Cerebral hemodynamics in ischemic cerebrovascular disease. Ann Neurol 29: 231-40, 1991
15) van Mook WN, Rennenberg RJ, Schurink GW, et al: Cerebral hyperperfusion syndrome. Lancet Neurol 4: 877-88, 2005
16) Heros RC, Scott RM, Kistler JP, et al: Temporary neurological deterioration after extracranial-intracranial bypass. Neurosurgery 15: 178-85, 1984
17) Kontos HA, Raper AJ, Patterson JL: Analysis of vasoactivity of local ph, pco2 and bicarbonate on pial vessels. Stroke 8: 358-60, 1977
18) Wahl M, Deetjen P, Thurau K, et al: Micropuncture evaluation of the importance of perivascular ph for the arteriolar diameter on the brain surface. Pflugers Arch 316: 152-63, 1970
19) Hosoda K, Kawaguchi T, Shibata Y, et al: Cerebral vasoreactivity and internal carotid artery flow help to identify patients at risk for hyperperfusion after carotid endarterectomy. Stroke 32: 1567-73, 2001
20) Matsubara S, Moroi J, Suzuki A, et al: Analysis of cerebral perfusion and metabolism assessed with positron emission tomography before and after carotid artery stenting. J Neurosurg 111: 28-36, 2009
21) Nariai T, Matsushima Y, Imae S, et al: Severe haemodynamic stress in selected subtypes of patients with moyamoya disease: A positron emission tomography study. J Neurol Neurosurg Psychiatry 76: 663-9, 2005
22) Ogasawara K, Yukawa H, Kobayashi M, et al: Prediction and monitoring of cerebral hyperperfusion after carotid endarterectomy by using single-photon emission computerized tomography scanning. J Neurosurg 99: 504-10, 2003
23) Folbergrova J, Ingvar M, Siesjo BK: Metabolic changes in cerebral cortex, hippocampus, and cerebellum during sustained bicuculline-induced seizures. J Neurochem 37: 1228-38, 1981
24) Brodersen P, Paulson OB, Bolwig TG, et al: Cerebral hyperemia in electrically induced epileptic seizures. Arch Neurol 28: 334-8, 1973
25) Katsura K, Folbergrova J, Gido G, et al: Functional, metabolic, and circulatory changes associated with seizure activity in the postischemic brain. J Neurochem 62: 1511-5, 1994
26) Suh M, Ma H, Zhao M, et al: Neurovascular coupling and oximetry during epileptic events. Mol Neurobiol 33: 181-97, 2006
27) Theodore WH, Balish M, Leiderman D, et al: Effect of seizures on cerebral blood flow measured with 15o-h2o and positron emission tomography. Epilepsia 37: 796-802, 1996
28) Marchal G, Young AR, Baron JC: Early postischemic hyperperfusion: Pathophysiologic insights from positron emission tomography. J Cereb Blood Flow Metab 19: 467-82, 1999
29) Ito H, Kanno I, Fukuda H: Human cerebral circulation: Positron emission tomography studies. Ann Nucl Med 19: 65-74, 2005
30) JET study Group: Japanese EC-IC bypass Trial (JET study) : study design and interim analysis. Surg Cereb Stroke 30: 97-100, 2002

Experimental Pig Model of Old Myocardial Infarction with Long Survival Leading to Chronic Left Ventricular Dysfunction and Remodeling as Evaluated by PET

Noboru Teramoto[1], Kazuhiro Koshino[1], Ikuo Yokoyama[2,3], Shigeru Miyagawa[4], Tsutomu Zeniya[1], Yoshiyuki Hirano[1], Hajime Fukuda[1], Junichiro Enmi[1], Yoshiki Sawa[4], Juhani Knuuti[5], and Hidehiro Iida[1]

[1]Department of Investigative Radiology, National Cerebral and Cardiovascular Center Research Institute, Osaka, Japan; [2]School of Medicine and Faculty of Medicine, University of Tokyo, Tokyo, Japan; [3]Department of Cardiovascular Medicine, Sanno Hospital, International University of Health and Welfare, Tokyo, Japan; [4]Department of Cardiac Surgery, Osaka University, School of Medicine, Osaka, Japan; and [5]Turku PET Centre, University of Turku, Turku, Finland

A pig model of reduced left ventricular (LV) function and remodeling or chronic heart failure with long survival after myocardial infarction (MI) has not been established. The aim of this study was to evaluate the pathophysiologic status of a pig model of old MI using a series of PET studies. **Methods:** Twenty-seven male farm pigs were divided into 2 groups: 7 animals in the control group and 20 animals that underwent a proximal coronary artery (CA) occlusion using an ameroid constrictor after distal CA ligation. A series of PET examinations was performed to assess LV volumes, LV functions, myocardial perfusion response to adenosine, and viability as water-perfusable tissue index. **Results:** The distal CA ligation inhibited arrhythmia during and after the operation, and a transmural anteroseptal MI, with an infarction area of 27% ± 5% of the whole left ventricle, was generated with a survival rate of 75% at 4 mo. Wall motion evaluated by ^{18}F-FDG PET was diffusely reduced, including the noninfarcted wall. Global LV ejection fraction as assessed by gated C^{15}O PET was reduced (39% ± 16%) in the group undergoing occlusion, compared with the control group (66% ± 16%, $P < 0.05$). LV end-systolic (31.4 ± 9.2 cm^3) and end-diastolic (52.7 ± 10.2 cm^3) volumes were increased, compared with controls (15.2 ± 9.4 cm^3, $P < 0.01$, and 41.7 ± 11.5 cm^3, $P < 0.05$, respectively). Histology showed hypertrophy and development of microscopic fibrosis in noninfarcted myocardium. PET demonstrated the reduced myocardial perfusion response to adenosine and also reduced water-perfusable tissue index in remote segments. **Conclusion:** The pig model of old MI generated by the chronic proximal CA obstruction after distal ligation was characterized by LV dysfunction and remodeling, with a high survival rate.

Key Words: experimental model; PET; myocardial flow reserve; remodeling; regeneration therapy

J Nucl Med 2011; 52:761–768
DOI: 10.2967/jnumed.110.084848

Received Oct. 30, 2010; revision accepted Dec. 9, 2010.
For correspondence or reprints contact: Hidehiro Iida, Department of Investigative Radiology, National Cardiovascular Center Research Institute, 5-7-1 Fujishiro-dai, Suita City, Osaka, Japan 565-8565.
E-mail: iida@ri.ncvc.go.jp

Chronic heart failure (CHF) is an increasing health concern (*1*). Myocardial infarction (MI) is the cause of CHF in two thirds of the patients, and the morbidity and mortality remain high (*2,3*). The potential therapies, such as new class of pharmacologic agents and cell therapy (*4*), need to be tested in proper animal models to demonstrate the effects and outcome before initiating clinical trials. Dogs have been extensively used in heart research. Because the coronary arterial systems in dogs can develop collaterals quickly when myocardial ischemia occurs, it has been difficult to produce a large MI that typically introduces CHF with general characteristics of left ventricular (LV) remodeling (*5*).

Pigs have been considered better suited than dogs for pathophysiologic research of ischemic heart diseases, because the coronary system of pigs is more similar to that of humans (*6*). Tolerance of ischemia and denervation after ischemia in pigs is also similar to that in humans (*6*). Because of the delayed development of collaterals after occlusion, ligation of a peripheral part of the coronary arterial system generates a small MI (*7*). However, an experimental model of large MI introducing global LV dysfunction is difficult to develop, because sudden cardiac death (SCD) due to fatal arrhythmias and an intolerance of ischemia frequently occurs in pigs (*8*). The models of small MI made by the ligation of a peripheral part of the coronary arterial system demonstrate reasonably good survival rates but only for a small infarction. The model of small MI using a coronary ameroid constrictor (model MRI-2.50-TI; Research Instruments SW) has also demonstrated moderate SCD rates (*6,8–13–15*), but the animals develop primarily chronic ischemia or hibernating myocardium, without a significant amount of scar tissue. Thus, the limitations of current models are that the infarcted region is small and that the hearts are not developing a clinical picture of CHF with global LV dysfunction, LV dilatation, and remodeling.

On the other hand, Shen et al. (*16*) developed an experimental pig model of MI and heart failure. Sequential

ligation of distal and proximal coronary arteries was used to establish MI with a reasonable survival rate, and pacing tachycardia was used to achieve heart failure. However, this pig model was studied over only a short term (21 d) and required pacing tachycardia to cause CHF. There has been little evaluation of pathophysiology and no evidence of the presence of cardiac remodeling.

This aim of this study was to characterize the pig model of old MI. We first reinvestigated the technique of generating a pig model of relatively large MI causing global LV dysfunction and LV remodeling in segments remote from the infarcted region, by means of the sequential ligation of distal and proximal coronary arteries without the pacing procedures. We then evaluated the pathophysiologic characteristics of this animal model by comprehensively analyzing histology, LV volumes and LV function, myocardial perfusion response to adenosine, and perfusable tissue fractions (PTF) in the remote segment, using an advanced PET technique.

MATERIALS AND METHODS

Subjects

Male farm pigs, 3 mo old at the start of the study (weight range, 18–23 kg; mean weight ± SD, 20 ± 1.2 kg), were used. The animals were divided into 2 groups. Group A consisted of 7 pigs without any operation and was designated as the control group (average body weight, 26 ± 2.4 kg). Group B consisted of 20 pigs that underwent occlusion using an ameroid constrictor (*7*); ligation of the distal left anterior descending coronary artery (LAD) was performed before the ameroid constrictor was used. Of the 16 pigs that survived for 4 mo after the operation, 7 underwent PET studies. The other 9 were assigned to tissue-regenerative projects. The average body weight of this group of 7 pigs was 42 ± 8.2 kg at the time of the PET scan.

Animals were maintained and handled in accordance with guidelines for animal research (*17*). The study protocol was approved by the local Committee for Laboratory Animal Welfare, National Cardiovascular Center, Osaka, Japan.

Permanent Occlusion Procedures

In group B, permanent occlusion was made at the proximal LAD using an ameroid constrictor (*18*) (Fig. 1) as follows. Pigs were preanesthetized by an intramuscular injection of ketamine hydrochloride (20 mg/kg; Ketaral [Diichi-Sankyo]) and xylazine hydrochloride (2 mg/kg; Celactal [Bayer HealthCare]). The animals were positioned supine, and a 22-gauge indwelling needle (Surflo F&F; Terumo) was inserted in the central vein of the auricle. A 3-way cock (Terufusion TS-TR2K; Terumo) was attached to the external cylinder of the indwelling needle and connected for continuous anesthetic injection. The animals were intubated with an endotracheal cannula (6 French; Sheridan) and then connected to an artificial respirator (Single Animal Volume Controlled Ventilators model 613 [Harvard Apparatus]) with a stroke volume of 200–300 cm^3/stroke and frequency of 20/min. Propofol (6 mg/kg/h; Diprivan [Astra-Zeneca]) and vecuronium bromide (0.05 mg/kg/h; Musculux [Sankyo Yell Yakuhin Co., Ltd.]) were continuously infused using a syringe pump (Terufusion TE-3310N; Terumo). Then, the animals were fixed in a recumbent position so that the left thorax was exposed, and the outer layer of skin and muscles between the third and fourth ribs was dissected. The distance between the third and fourth ribs was widened with a rib spreader to allow a direct view of the left auricle and LAD. The pericardium was dissected along the LAD, from the upper part of the left auricle (~6 cm), to expose the myocardium around the LAD. The LAD on the proximal side, below the left auricle from the myocardium, was exfoliated for approximately 1 cm. A lidocaine hydrochloride jelly (Xylocaine jelly; Astra-Zeneca) was applied to anesthetize the area.

A complete ligation was first made on the distal LAD (no. 9), immediately after the second diagonal branch, using a suture (2-0; Nescosuture) approximately 20 min before the ameroid constrictor was fastened. An ameroid constrictor (COR-2.50-SS; Research Instruments) was then fastened using sutures as displayed in Figure 1. To enhance the effect of the ameroid constrictor, 2 additional suture strings were loosely rounded at the site of the ameroid so that these strings were located between (below) the ameroid constrictor and arterial wall.

PET Procedures

After fasting overnight, the pigs were sedated with ketamine hydrochloride (20 mg/kg) and xylazine hydrochloride (2 mg/kg) by intramuscular injection. Anesthesia was induced and maintained with intravenous propofol (6 mg/kg/h) and vecuronium bromide (0.05 mg/kg/h). The animals were intubated and mechanically ventilated with a mixture of 25% oxygen and 75% nitrogen at 10 mL/kg plus 50 mL/stroke at 20 strokes/min. Catheters were placed in the femoral artery to monitor the arterial blood pressure and in the femoral vein to infuse $H_2{}^{15}O$ or ^{18}F-labeled FDG. Systolic and diastolic blood pressure, heart rate, and arterial blood gases were monitored.

A series of PET scans was obtained using an ECAT-HR tomograph (CTI Inc.). The blood-pool images were obtained after the animals inhaled 2.7 GBq of $C^{15}O$ gas (*19*). Arterial blood samples were taken every minute during the $C^{15}O$ scan, and their radioactivity concentration in the whole blood was measured. Additional electrocardiogram-gated $C^{15}O$ images were obtained (16 gates). After 12–15 min of ^{15}O radioactivity decay, 7 dynamic $H_2{}^{15}O$ PET scans were acquired at intervals of 12–15 min. The first and the last scans were obtained without pharmacologic stress, and the second through sixth scans were obtained during intravenous infusion of adenosine (100, 200, 400, 600, and 800

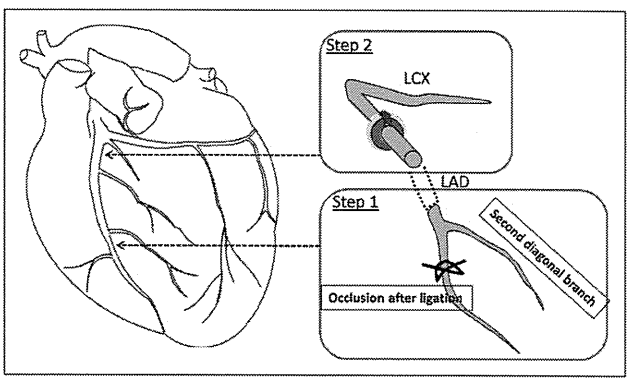

FIGURE 1. Ligation of LV LAD. Distal LAD after second diagonal branch was ligated, and 30 min later ameroid constrictor was placed at proximal LAD. Two suture strings were inserted between ameroid constrictor and arterial wall to make occlusion complete. LCX = left circumflex artery.

[only for group A] μg/kg/min). The 6-min dynamic scan of 26 frames (12 × 5, 8 × 15, and 6 × 30 s) was started when radioactivity appeared in the right ventricle. Furthermore, another PET scan using ^{18}F-FDG was acquired using a euglycemic hyperinsulinemic clamp (*20,21*). For this study, insulin (4 mIU/kg/h) and glucose (5–8 mg/kg/min) were continuously infused over 2 h, and then approximately 111 MBq of ^{18}F-FDG was intravenously injected. The blood glucose was 109 ± 10.6, 105 ± 3.8, and 107 ± 10.0 mg/dL at the time of ^{18}F-FDG injection. PET images were acquired dynamically for 60 min, and the images acquired during the last 30 min were used for further analysis. An additional electrocardiogram-gated scan was obtained for 30 min to estimate myocardial wall motion and wall thickening.

After the PET scans, coronary angiography was undertaken to confirm the occlusion of LAD. A portable angiographic camera (Digital Mobile Imaging System OEC Series 9800; GE Healthcare U.K. Ltd.) was used with the contrast medium (Omnipaque 300; Daiichi-Sankyo).

Histologic Analysis

At the end of the study, pentobarbital sodium was administered, and animals were euthanized. The animals' hearts were then excised and sliced at a thickness of 10 mm to correspond to PET images (*22*). The slices were stained with Masson trichrome and hematoxylin and eosin. The surface area of the infarcted LV wall on the stained slices was calculated according to a previously describe procedure (*22*). The length of the infarcted zone, including both transmural and nontransmural infarction, was measured on each of the stained slices along the LV wall. The defect surface area was then calculated as a summation of the defect length multiplied by the slice interval. The cell and microvascular structures were also analyzed. In particular, development of fibrosis, cell enlargement, and degeneration of the vascular network were visually estimated. The analysis was masked from the other analyses.

Data Analysis

The extravascular tissue density images (g/mL) were calculated by subtracting the $C^{15}O$ blood volume from the transmission images (*23*). The relative images of myocardial blood flow (MBF) and water-PTF (g/mL) were also generated from the dynamic $H_2{}^{15}O$ images (*22,23*). The relative accumulation of ^{18}F-FDG was calculated using validated techniques (*24*). The regions of interest were placed in the anterior wall and lateral–anterior wall, which corresponded to the MI and normal-tissue regions, respectively. The regions of interest were then copied to other images, and the quantitative parameters of regional MBF (mL/min/g), PTF (g/mL), and arterial blood volume V_a (mL/mL) were calculated using nonlinear least-squares fitting as described previously (*22,23*). These calculations were done for all $H_2{}^{15}O$ PET studies to estimate baseline MBF and the adenosine-based responses both in MI and in non-MI regions.

The water-perfusable tissue index (PTI) (*23,25,26*), which was defined as the fraction of water-perfusable tissue over total tissue, was calculated by dividing PTF by the extravascular tissue density images. This calculation was done for each myocardial region and compared between the infarcted anterior wall and normal posterior–lateral wall regions. The obtained values were also compared with control subjects.

The LV ejection fraction and cardiac output were evaluated by counting the total counts within the LV area from the typical electrocardiogram-gated $C^{15}O$ images shown in Figure 2. The wall motion was analyzed using electrocardiogram-gated ^{18}F-FDG images. The wall motion score was divided into 4 levels (normal, 0; hypokinetic, 1; akinetic, 2; and dyskinetic, 3) and defined for the anterior wall and contralateral (lateral–posterior) wall regions.

The surface area of the infarcted LV wall on the ^{18}F-FDG and PTF images was calculated as described previously (*22*). A significant defect was defined as a value less than 50% of that in the control region, which was defined in the contralateral region, indicating preserved ^{18}F-FDG, preserved PTF, and elevated MBF during adenosine. The myocardial midlines were then traced along the 50% of peak count boundary of the $C^{15}O$ blood volume images at each slice (*22*). The surface area of the defect was calculated as a summation of the defect length multiplied by the slice interval. These defect surface areas were compared with those obtained from the stained slices.

All data were presented as mean ± SD. Pearson correlation and linear regression analyses were used to evaluate relationships between the 2 values. A P value of less than 0.05 was considered statistically significant.

RESULTS

Survival Rates of Animal Groups

No adverse events were detected in group A; in group B, 4 pigs (20%) died within a month and an additional pig 1 mo after that. Thus, the total survival rate at 4 mo was 75% in group B. Severe arrhythmia occurred in all animals in group B during the operation. The arrhythmia and fibrillation, introducing the sudden cardiac death, were significantly suppressed at approximately 20 min after ligation of the distal LAD. Figure 3 displays the survival rates of the pigs that underwent the operation.

Of the pigs in group B that survived for 4 mo, 7 were selected for further characterization and imaging studies. These 7 animals were compared against the animals in group A, on which no operation was performed. The characteristics of the 2 groups at the time of the imaging

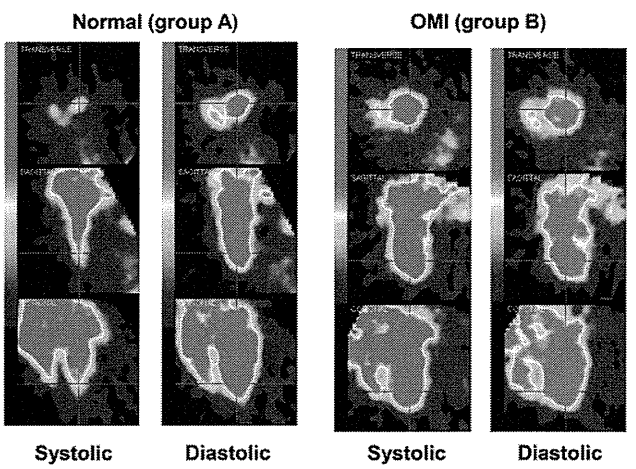

FIGURE 2. Typical images obtained from electrocardiogram-gated PET scans with $C^{15}O$ inhalation at end-systolic and end-diastolic phases. OMI = old MI.

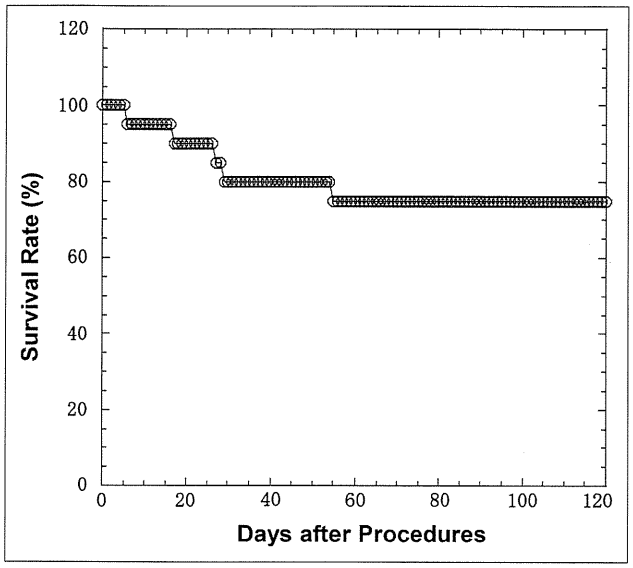

FIGURE 3. Survival rates for group B after ameroid constrictor was placed.

studies are displayed in Table 1. Because the animals in group B were allowed to grow after operation, they were larger at the time of the imaging studies.

Characteristics of Groups

Table 1 shows the hemodynamic data for the animals in groups A and B. Compared with group A, group B showed a significantly reduced heart rate and diastolic blood pressure and, thus, rate–pressure product. In addition, the global LV ejection fraction measured with gated $C^{15}O$ PET in group B was significantly reduced (39% ± 16% [24%–59%] in group B vs. 66% ± 16% [46%–91%] in group A, $P < 0.01$). LV end-systolic volume in group B was significantly increased (31.4 ± 9.2 cm^3 in group B vs. 15.2 ± 9.4 cm^3 in group A, $P < 0.01$), and LV end-diastolic volume was also significantly increased (52.7 ± 10.2 cm^3 in group B vs. 41.7 ± 11.5 cm^3 in group A, $P < 0.05$). Increased end-systolic and end-diastolic volumes are also clearly visible in Figure 2. Systolic blood pressure and diastolic blood pressure, as well as rate–pressure product, were reduced during adenosine study in both groups. Heart rate was increased in group A but not in group B. Other parameters such as hemoglobin concentration (g/dL), percentage saturation of arterial O_2, $PaCO_2$ (mm Hg), and PO_2 (mm Hg) were not significantly different between the 2 groups. Table 2 shows detailed hemodynamic parameters and the results from the histologic analysis for each individual animal in group B. Wall motion score was reduced (akinesis–dyskinesis or 2–3) in the anterior wall, which includes the area of MI. The wall motion score was also reduced diffusely in all animals and indicated hypokinesis (grade 1) in the infarct-remote posterolateral wall. The coronary angiography demonstrated complete occlusion of the LAD in all animals in group B. As shown in Figure 4, no clear collateral circulation existed.

Imaging Results

The myocardial perfusion ($H_2{}^{15}O$) and metabolism (^{18}F-FDG) images at the mid ventricular plane and their corresponding slices after histochemical staining for the animals in group B are displayed in Figure 5. In all animals, clear signs of MI were detected in the anterior wall. The surface area of the MI was 13.7 ± 4.3 cm^2, which corresponded to 27% ± 9% of the whole left ventricle. Both PTF and ^{18}F-FDG images visually agreed well with the stained slices. Moreover, the ^{18}F-FDG images agreed well with the qualitative PTF images in all animals. The spatial distribution and size of the developed MI are visually reproducible

TABLE 1
Physiologic Parameters of Pigs at Time of PET

Parameter	Group A (control, n = 7)	Group B (old MI, n = 7)
Body weight (kg)	26 ± 2.4	41 ± 8.2
Heart rate (beats·min^{-1})	72 ± 22.4 (82 ± 21.4*)	52 ± 6.3† (53 ± 9.2)
Systolic blood pressure (mm Hg)	131 ± 22.1 (95 ± 22.4‡)	111 ± 18.3† (97 ± 15.0*)
Diastolic blood pressure (mm Hg)	92 ± 19.3 (49 ± 16.7‡)	74 ± 13.6† (57 ± 11.9‡)
Rate pressure product (mm Hg·min^{-1})	9,567 ± 3,616 (5,657 ± 3201‡)	5,732 ± 1,151† (4,445 ± 948*)
Wall thickness (posterior–lateral wall) (cm)	1.2 ± 0.1	1.6 ± 0.1‡
End-diastolic LV volume (mL)	41.7 ± 11.5	52.73 ± 10.2†
End-systolic LV volume (mL)	15.2 ± 9.4	31.4 ± 9.2*
LV ejection fraction (%)	66.0 ± 16.2	39.7 ± 16.9*
Hemoglobin concentration (g/dL)	13 ± 1.5	12 ± 0.9
Saturation of arterial O_2 (%)	99 ± 1.0	99 ± 0.6
pCO_2 (mm Hg)	39 ± 2.7	41 ± 2.8
pO_2 (mm Hg)	125 ± 20.1	141 ± 11.4

*$P < 0.01$.
†$P < 0.05$.
‡$P < 0.001$.
Data are mean ± SD. Values in parentheses are from administration of maximum dose of adenosine.

TABLE 2
Hemodynamic Parameters of Pigs with Old MI (Group B)

Subject no.	BW (kg)	HR (beats·min^{-1})	SBP (mm Hg)	DBP (mm Hg)	RPP (mm Hg·min^{-1})	tHb (g/dL)	SAT (%)	pCO_2 (mm Hg)	pO_2 (mm Hg)	WM								
										Anterior wall	Posterior-lateral wall	WT (posterior-lateral wall)	EDV (mL)	ESV (mL)	EF (%)	LV surface area (cm^2)	MI surface area (cm^2)	DAF (%)
1	37	53	117	72	6,201	10.8	98.7	37.8	132	3	1	1.6	39.5	29.9	24.3	53.7	10.9	20.3
2	39	38	110	70	4,180	11.5	98.9	37	154.5	2	1	1.6	58.2	42.4	27.1	57	16.2	28.4
3	33	53	85	60	4,505	11.5	99.3	39.3	137.7	3	1	1.6	55.4	42.3	23.6	50	16	31.9
4	32	55	91	58	5,005	11.3	99.6	40.7	135.5	–	–	1.8	0	0	0	53.9	9.2	17.1
5	45	52	137	93	7,124	10.3	98.1	43.6	124.1	3	1	1.8	68.4	27.6	59.7	50	19.9	39.7
6	50	52	126	90	6,552	11.8	99.7	42.8	148.4	3	1	1.5	49.3	27.1	45	48.6	15.5	31.8
7	53	58	113	78	6,554	13.3	99	43.7	152.8	2	1	1.5	45.7	19.1	58.2	49.8	8.4	16.9
Mean	41	52	111	74	5,732	12	99	41	141	2.7	1	1.6	52.7	31.4	39.7	51.9	13.7	26.6
SD	8.2	6.3	18.3	13.6	1,151	0.9	0.6	2.8	11.4	0.5	0	0.1	10.2	9.2	16.9	3.05	4.3	8.7

BW = body weight; HR = heart rate; SBP = systolic blood pressure; DBP = diastolic blood pressure; RPP = rate–pressure product; tHB = hemoglobin concentration; SAT = saturation of arterial O_2; WM = wall motion; WT = wall thickness; EDV = end-diastolic LV volume; ESV = end-systolic LV volume; EF = ejection fraction; DAF = defect area fraction.

FIGURE 4. Example of coronary angiogram in animal with ameroid constrictor (arrow) (group B).

among the animals. Myocardial hypertrophy was visible in the wall regions remote from the infarcted area. In group B, the posterior–lateral wall thickness estimated from histochemical staining was 16 ± 1 mm (Table 2), which was significantly greater than that of group A (12 ± 1 mm; Table 1) ($P < 0.001$).

Further analysis of the size of the infarcted region is displayed in Figure 5B. We excluded 1 animal whose ^{18}F-FDG PET images demonstrated high accumulation at the anterior LV area (and therefore a smaller value in the defect surface area), which was attributed to the adhesion or inflammation between the myocardial and chest walls. Thus, the defect area on histology showed intersubject variation of approximately 20%. The results of both ^{18}F-FDG and PTF image analysis and histochemical analysis agreed well (Fig. 5B). Baseline and adenosine-stimulated MBF were also clearly blunted in the anterior wall in the animals in group B (Fig. 6A). Interestingly, abnormally reduced adenosine flow response also was detected in the myocardial regions remote from the MI in group B, whereas the baseline flow values were normal.

Further analysis of myocardial PTF and PTI values—indices of PTF—revealed that these values were significantly reduced in the infarcted anterior wall in group B (Fig. 6B). PTI was also moderately but significantly (~10%) reduced in the remote myocardial wall in group B.

Histologic Analysis

Histologic analysis did not show any signs of MI in group A, but transmural anterior wall MI was apparent in all animals in group B. Hypertrophy was detected in the posterior wall of group B in all animals. Multinuclear muscle cell breeding (Fig. 7A) and hyperplasia of blood vessels (Fig. 7B) were also visible in all animals in group B, mostly in the subendocardial regions. Denaturation necrosis with epicardial fibrous change and hypertrophy has also been seen in the lateral–posterior wall regions of group B (Fig. 7C).

DISCUSSION

This study demonstrated that 75% of pigs with old MI generated by the 2 steps of LAD ligation survived more than 4 mo. Such a long survival has never, to our

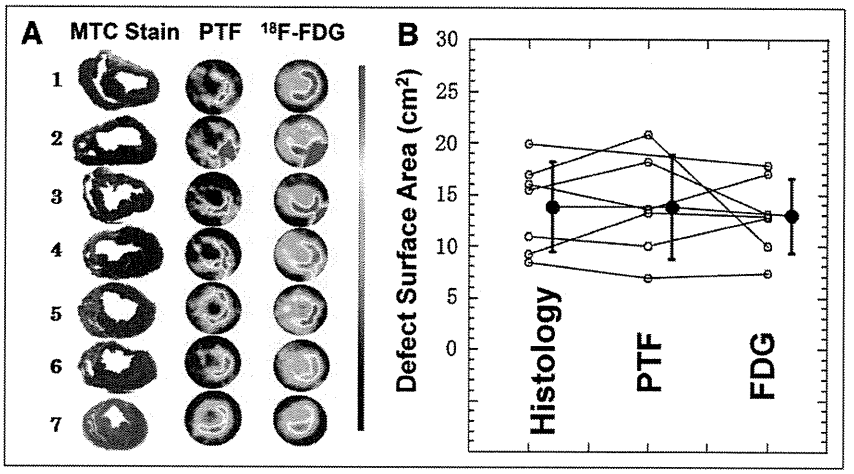

FIGURE 5. (A) Histologic, PTF, and ^{18}F-FDG slices at middle level of left ventricle in 7 animals of group B. Spatial distribution and size of MI are visually reproducible among animals. Myocardial hypertrophy was visible in remote myocardial wall regions. (B) Comparison of defect surface areas obtained from histologic stained slices with PET images using ^{18}F-FDG and PTF. MTC = Masson trichrome.

knowledge, been accomplished in any studies of pig heart disease. The size of MI reached approximately 27% of the whole left ventricle, causing the remodeling and global LV dilatation (significantly increased LV end-systolic and end-diastolic volumes) to be associated with reduced global LV function. PET with $C^{15}O$ and ^{18}F-FDG showed that regional LV wall motion was impaired not only in the infarcted region but also in the myocardial areas remote from the MI. PET also demonstrated reduced MBF reactivity in remote regions in addition to the infarct area. PTI was also reduced in the remote region, suggesting development of microscopic fibrosis. Moreover, other findings from histology indicated the existence of abnormalities in the noninfarcted area remote from the MI. These results indicate that this animal model may be close to human CHF after MI.

Shen et al. (*16*) adopted additional pacing tachycardia in pigs after sequential coronary artery ligations and observed global LV dysfunction, claiming that CHF was introduced. The present study is similar to the study by Shen et al. (*16*) but is based on only sequential coronary artery obstructions accomplished with acute distal coronary artery occlusion followed by a chronic proximal coronary occlusion with an ameroid constrictor, causing similar LV dysfunction. Of note was the better survival rate (80% at 1 mo, 75% at 4 mo) demonstrated in the current report than in any previous report (*6,8–12,14,16*), including Shen et al. (73.3% at 21 d). In addition, it has not been confirmed whether such a good survival rate at 21 d could last more than 4 mo after producing global LV dysfunction with MI. Our preliminary experiment, independently performed on 69 farm pigs, demonstrated that when the proximal LAD was occluded by the ameroid constrictor alone, 45 pigs (65%) died within a month, and the total survival rate was 30% at 4 mo. This survival rate is significantly smaller than the rates from the present study.

The reason why animals with MI acquired such good survival is not fully understood. However, it was clearly observed that the ligation of the peripheral coronary artery before the gradual occlusion of the main trunk of the LAD apparently inhibited the fibrillation during the operation. This procedure is obviously effective at protecting against

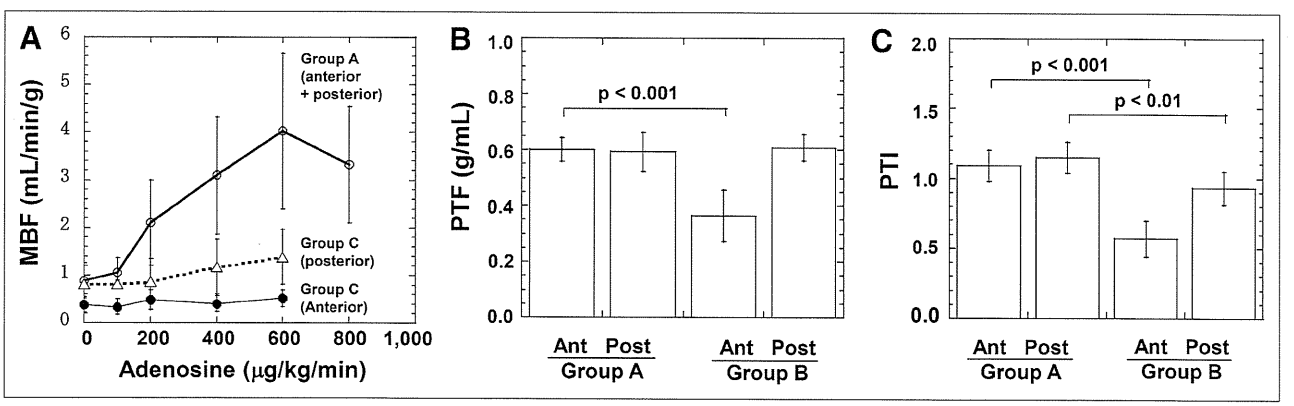

FIGURE 6. Results from PET studies. (A) Regional MBF as function of adenosine dose. In group A, MBF increases with increasing adenosine dose. In infarcted anterior wall of group B, MBF is reduced at rest and does not respond to adenosine. In posterior wall region, adenosine reactivity was significantly reduced. (B and C) Comparison of water-PTF (B) and water-PTI (C). Both were reduced in anterior wall of group B. PTI was also reduced in posterior wall in group B. Ant = anterior; Post = posterior.

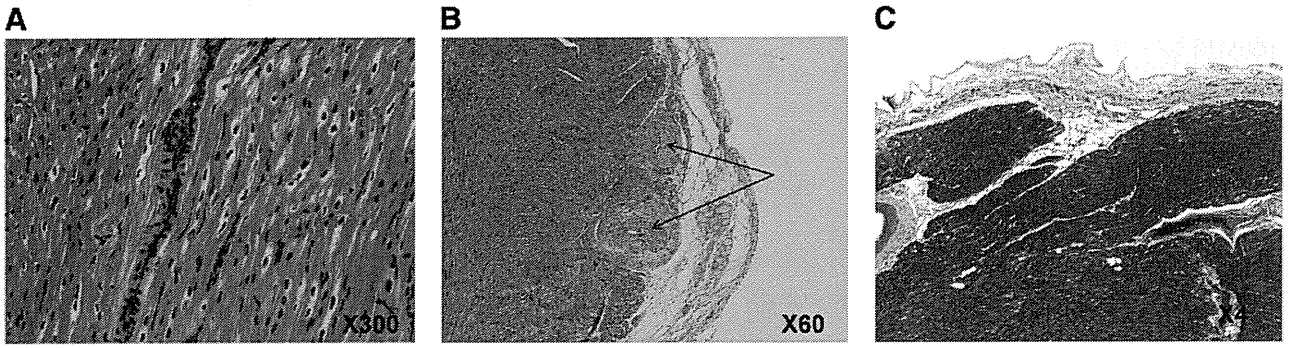

FIGURE 7. Typical images of histologic staining obtained from group B. Hypertrophy with multinuclear muscle cell breeding (A), hyperplasia of blood vessels shown as arrows (B), and denaturation necrosis often seen in subendocardial regions, as in this picture (C), are typical findings.

fatal arrhythmias. This preconditioning effect is supported by the experiments of Moses et al. (*27*), in which ischemic preconditioning of the distal coronary artery protected cardiac muscle through a mechanism involving the potassium channels of mitochondria and myocytes. There may be contributions from other preconditioning factors (*9,28–30*) that associate with increased tolerance of ischemia. Another mechanism could be associated with the modulation of sympathetic tone. It has been reported that regional heterogeneity in myocardial cellular mechanisms (responsible for myocardial cellular depolarization) and repolarization in hibernating myocardium (*12*) can induce ventricular fibrillation (*9*). Inhibition of such heterogeneous myocardial cellular mechanisms or control of modulated sympathetic tone could be another possible explanation.

The present study used a gradual total occlusion of the proximal of LAD, as evidenced by the coronary angiography (Fig. 4), and thus caused an MI of approximately 27% of the total myocardium. The global LV ejection fraction in group B was significantly reduced (39% vs. 66% in controls), showing that LV systolic function was impaired in group B. Both histology and PET had concordant findings. The baseline MBF in the MI area was reduced and was not responding to adenosine administration. This finding is reasonable because the infarcted tissue should have reduced capillary density, and the resistive vessels do not respond to any vasodilating stimulation. The physical extent and size of the MI were reproducible among the individual animals. This feature is important when this animal model is applied to evaluate various new pharmaceuticals or various regenerative therapeutic trials.

The noninfarcted myocardium developed clear signs of remodeling, such as hypokinesis, hypertrophy, and the accumulation of fibrotic tissue in the remote myocardial wall, and significantly decreased PTI values, a marker of residual fractionation of water-perfusable tissue. The baseline MBF was preserved, but reactivity to the adenosine was blunted, even at a maximum dose of 600 μg/kg/min. This reduced reactivity could be related to the degeneration of small arteries, possibly caused by enlargement of myocytes and development of moderate denaturation necrosis and fibrosis.

This study demonstrated that physiologic status and physical extent of MI can be evaluated using the noninvasive technique of PET. The defect surface area identified with ^{18}F-FDG was identical to that identified with PTF, and both agreed well with the results of histology. Furthermore, microscopic degeneration can be characterized as reduced reactivity of quantitative myocardial perfusion to adenosine. The PET-derived PTI, which is known to indicate the absolute fraction of non–scar tissue within the area (*22*), was reduced not only in the infarcted anterior wall but also in the remote region by 10%. As demonstrated in recent studies (*31–34*), the reduced PTI in a control region is thought to be caused by the development of microscopic fibrosis.

In this study, left-atrial and LV pressure analyses have not been measured, because the aims of this study were to create a long-survival pig model of MI and global LV dysfunction with remodeling, characterize this model using PET, and compare these parameters with histology before making a complete model of CHF after MI in pigs. One limitation of this study was that, because of technical reasons in our laboratory at the initiation of this study, it was difficult to measure left-atrial and LV pressures.

CONCLUSION

Our pig model of postinfarction global LV dysfunction was characterized by a high survival rate and large MI, with clear signs of cardiac remodeling, as demonstrated by PET and histology. This animal model might contribute to investigations of MI and new therapies for cardiac remodeling in MI.

ACKNOWLEDGMENTS

We thank the staff of the Department of Investigative Radiology of National Cardiovascular Center for invaluable technical assistance. This study was supported by a re-

search grant from New Energy and Industrial Technology Development Organization (NEDO), Japan, and grants for translational research and nanomedicine from the Ministry of Health, Labor and Welfare (MHLW), Japan.

REFERENCES

1. Saito·I, Folsom AR, Aono H, Ozawa H, Ikebe T, Yamashita T. Comparison of fatal coronary heart disease occurrence based on population surveys in Japan and the USA. *Int J Epidemiol.* 2000;29:837–844.
2. Balady GJ, Jette D, Scheer J, Downing J. Changes in exercise capacity following cardiac rehabilitation in patients stratified according to age and gender: results of the Massachusetts Association of Cardiovascular and Pulmonary Rehabilitation Multicenter Database. *J Cardiopulm Rehabil.* 1996;16:38–46.
3. Krum H, Haas SJ, Eichhorn E, et al. Prognostic benefit of beta-blockers in patients not receiving ACE-inhibitors. *Eur Heart J.* 2005;26:2154–2158.
4. Anversa P, Leri A, Kajstura J. Cardiac regeneration. *J Am Coll Cardiol.* 2006;47:1769–1776.
5. Gheeraert PJ, Henriques JP, De Buyzere ML, De Pauw M, Taeymans Y, Zijlstra F. Preinfarction angina protects against out-of-hospital ventricular fibrillation in patients with acute occlusion of the left coronary artery. *J Am Coll Cardiol.* 2001;38:1369–1374.
6. Millard RW. Induction of functional coronary collaterals in the swine heart. *Basic Res Cardiol.* 1981;76:468–473.
7. Roth DM, Maruoka Y, Rogers J, White FC, Longhurst JC, Bloor CM. Development of coronary collateral circulation in left circumflex Ameroid-occluded swine myocardium. *Am J Physiol.* 1987;253:H1279–H1288.
8. Fallavollita JA, Riegel BJ, Suzuki G, Valeti U, Canty JM Jr. Mechanism of sudden cardiac death in pigs with viable chronically dysfunctional myocardium and ischemic cardiomyopathy. *Am J Physiol Heart Circ Physiol.* 2005;289:H2688–H2696.
9. Canty JM Jr, Suzuki G, Banas MD, Verheyen F, Borgers M, Fallavollita JA. Hibernating myocardium: chronically adapted to ischemia but vulnerable to sudden death. *Circ Res.* 2004;94:1142–1149.
10. Fallavollita JA, Canty JM Jr. Differential ^{18}F-2-deoxyglucose uptake in viable dysfunctional myocardium with normal resting perfusion: evidence for chronic stunning in pigs. *Circulation.* 1999;99:2798–2805.
11. Fallavollita JA, Canty JM Jr. Ischemic cardiomyopathy in pigs with two-vessel occlusion and viable, chronically dysfunctional myocardium. *Am J Physiol Heart Circ Physiol.* 2002;282:H1370–H1379.
12. Fallavollita JA, Logue M, Canty JM Jr. Stability of hibernating myocardium in pigs with a chronic left anterior descending coronary artery stenosis: absence of progressive fibrosis in the setting of stable reductions in flow, function and coronary flow reserve. *J Am Coll Cardiol.* 2001;37:1989–1995.
13. Shen YT, Vatner SF. Mechanism of impaired myocardial function during progressive coronary stenosis in conscious pigs: hibernation versus stunning? *Circ Res.* 1995;76:479–488.
14. Mills I, Fallon JT, Wrenn D, et al. Adaptive responses of coronary circulation and myocardium to chronic reduction in perfusion pressure and flow. *Am J Physiol.* 1994;266:H447–H457.
15. Roth DM, White FC, Nichols ML, Dobbs SL, Longhurst JC, Bloor CM. Effect of long-term exercise on regional myocardial function and coronary collateral development after gradual coronary artery occlusion in pigs. *Circulation.* 1990;82:1778–1789.
16. Shen YT, Lynch JJ, Shannon RP, Wiedmann RT. A novel heart failure model induced by sequential coronary artery occlusions and tachycardiac stress in awake pigs. *Am J Physiol.* 1999;277:H388–H398.
17. *Guide for the Care and Use of Laboratory Animals.* Washington, DC: National Academy Press; 1996.
18. O'Konski MS, White FC, Longhurst J, Roth D, Bloor CM. Ameroid constriction of the proximal left circumflex coronary artery in swine: a model of limited coronary collateral circulation. *Am J Cardiovasc Pathol.* 1987;1:69–77.
19. Iida H, Takahashi A, Tamura Y, Ono Y, Lammertsma AA. Myocardial blood flow: comparison of oxygen-15-water bolus injection, slow infusion and oxygen-15-carbon dioxide slow inhalation. *J Nucl Med.* 1995;36:78–85.
20. DeFronzo RA, Tobin JD, Andres R. Glucose clamp technique: a method for quantifying insulin secretion and resistance. *Am J Physiol.* 1979;237:E214–E223.
21. Knuuti MJ, Nuutila P, Ruotsalainen U, et al. Euglycemic hyperinsulinemic clamp and oral glucose load in stimulating myocardial glucose utilization during positron emission tomography. *J Nucl Med.* 1992;33:1255–1262.
22. Iida H, Tamura Y, Kitamura K, Bloomfield PM, Eberl S, Ono Y. Histochemical correlates of ^{15}O-water-perfusable tissue fraction in experimental canine studies of old myocardial infarction. *J Nucl Med.* 2000;41:1737–1745.
23. Iida H, Rhodes CG, de Silva R, et al. Myocardial tissue fraction: correction for partial volume effects and measure of tissue viability. *J Nucl Med.* 1991;32:2169–2175.
24. Iida H, Rhodes CG, de Silva R, et al. Use of the left ventricular time-activity curve as a noninvasive input function in dynamic oxygen-15-water positron emission tomography. *J Nucl Med.* 1992;33:1669–1677.
25. de Silva R, Yamamoto Y, Rhodes CG, et al. Preoperative prediction of the outcome of coronary revascularization using positron emission tomography. *Circulation.* 1992;86:1738–1742.
26. Yamamoto Y, de Silva R, Rhodes CG, et al. A new strategy for the assessment of viable myocardium and regional myocardial blood flow using ^{15}O-water and dynamic positron emission tomography. *Circulation.* 1992;86:167–178.
27. Moses MA, Addison PD, Neligan PC, et al. Inducing late phase of infarct protection in skeletal muscle by remote preconditioning: efficacy and mechanism. *Am J Physiol Regul Integr Comp Physiol.* 2005;289:R1609–R1617.
28. Kitakaze M, Node K, Minamino T, et al. Role of activation of protein kinase C in the infarct size-limiting effect of ischemic preconditioning through activation of ecto-5′-nucleotidase. *Circulation.* 1996;93:781–791.
29. Kharbanda RK, Mortensen UM, White PA, et al. Transient limb ischemia induces remote ischemic preconditioning in vivo. *Circulation.* 2002;106:2881–2883.
30. Chen PS, Chen LS, Cao JM, Sharifi B, Karagueuzian HS, Fishbein MC. Sympathetic nerve sprouting, electrical remodeling and the mechanisms of sudden cardiac death. *Cardiovasc Res.* 2001;50:409–416.
31. Knaapen P, Boellaard R, Gotte MJ, et al. Perfusable tissue index as a potential marker of fibrosis in patients with idiopathic dilated cardiomyopathy. *J Nucl Med.* 2004;45:1299–1304.
32. Knaapen P, Boellaard R, Gotte MJ, et al. The perfusable tissue index: a marker of myocardial viability. *J Nucl Cardiol.* 2003;10:684–691.
33. Knaapen P, Bondarenko O, Beek AM, et al. Impact of scar on water-perfusable tissue index in chronic ischemic heart disease: evaluation with PET and contrast-enhanced MRI. *Mol Imaging Biol.* 2006;8:245–251.
34. Knaapen P, van Dockum WG, Bondarenko O, et al. Delayed contrast enhancement and perfusable tissue index in hypertrophic cardiomyopathy: comparison between cardiac MRI and PET. *J Nucl Med.* 2005;46:923–929.

TISSUE ENGINEERING: Part A
Volume 17, Numbers 15 and 16, 2011

DOI: 10.1089/ten.tea.2010.0482

Long-Term *In Vivo* Magnetic Resonance Imaging Tracking of Endothelial Progenitor Cells Transplanted in Rat Ischemic Limbs and Their Angiogenic Potential

Carlos A. Agudelo, Ph.D.,[1] Yoichi Tachibana, Ph.D.,[1] Teramoto Noboru, B.Sc.,[2] Hidehiro Iida, Ph.D.,[2] and Tetsuji Yamaoka, Ph.D.[1,3]

Stem cell therapy has been used to repair ischemic tissues in the limbs, in myocardial infarctions, and in the brain. To understand the mechanisms of healing, a contrast agent capable of inducing sufficient magnetic resonance (MR) contrast would be useful in providing fundamental information about the cell migration and incorporation into the ischemic tissue. A magnetic resonance imaging contrast agent composed of dextran and gadolinium chelate was synthesized. Hydroxyl groups of dextran were activated with 1,1′-carbonylbis-1H-imidazole and reacted with propanediamine to obtain aminated dextran. This modified polymer was then reacted with mono-N-succinimidyl 1,4,7,10-tetraazacyclododecane-1,4,7,10-tetraacetate, then with fluorescein isothiocyanate, and finally reacted with gadolinium chloride solution (Dex-DOTA-$Gd3^+$). Endothelial progenitor cells (EPCs) were selected as a stem cell model for magnetic resonance imaging tracking. Cells were isolated from the bone marrow harvested from the femurs and tibias of rats. Dex-DOTA-$Gd3^+$ was then introduced into the EPCs by electroporation. The intracellular stability and cytotoxicity of Dex-DOTA-$Gd3^+$ were evaluated *in vitro*. Dex-DOTA-$Gd3^+$-labeled EPCs were transplanted into a rat model of ischemic limb, and MR images were acquired. Dex-DOTA-$Gd3^+$ was found to efficiently label EPCs over a long duration without significant cytotoxicity. This provides an MR signal sufficient for tracking the EPCs intramuscularly injected into the limb.

Introduction

RECENT PROGRESS IN STEM CELL isolation from different sources such as blood, bone marrow (BM), and adipose tissue, coupled with better understanding of their functions, has led to the development of new applications of stem cell transplantation therapies in areas such as cardiac regeneration,[1,2] hind limb ischemia,[3–5] and stroke.[6] When implanting stem cells in ischemic tissues, the cells will likely differentiate into functional cells or release growth factors that act in a paracrine manner.[7–9] A system for tracking the stem cells *in vivo* would provide insights into many basic and practical questions related to stem cell therapy, such as the mechanisms involved in migration, recruitment, mobilization, and incorporation of cells into tissue.[7] Magnetic resonance imaging (MRI) is a noninvasive method that has the potential to reach the levels of sensitivity and resolution, which are necessary for detection of small quantities of cells and to determine their locations within ischemic tissues.

MRI tracking of cells labeled with iron oxide-based magnetic contrast agents has been used for visualization of many aspects of angiogenesis in different cell types such as the hematopoietic and neural progenitor cells.[10–12] One of the advantages of labeling cells with superparamagnetic iron oxide particles (SPIO) is the high sensitivity obtained compared with that obtained with other contrast agents.[13] Wilhelm *et al.* reported that SPIO-labeled cells can be detected in small quantities (30–60 cells in agarose gel) by high-resolution MRI.[14] Other studies reported stem cell homing to the organs and the BM,[15] differentiation and migration of oligodendrocyte progenitors into brain parenchyma, migration and incorporation of labeled cells to the sites of tumor angiogenesis,[16] and magnetic guiding of the endothelial progenitor cells (EPCs) to a target site.[14] However, despite the great advantages provided by SPIO labeling, some studies have reported certain disadvantages. Magnetic resonance (MR) signals in iron oxide-labeled cells transplanted into a mouse hind limb did not show significant differences from the day 1 to 28 post-transplantation; however, there is evidence for a progressive decrease in the cell number when monitored using genetically introduced bioluminescent signals.

Histological analysis confirmed that macrophages loaded with iron oxide particles were located between muscle

[1]Department of Biomedical Engineering, and [2]Department of Investigative Radiology Advanced Medical Engineering Center, National Cerebral and Cardiovascular Center Research Institute, Suita, Osaka, Japan.
[3]Japanese Science and Technology Agency–Core Research of Evolutional Science and Technology, Chiyoda-Ku, Tokyo, Japan.

bundles but no transplanted cells were detected near the macrophages.[15] Therefore, one of the problems when labeling with iron oxide is the instability to remain in the cells *in vivo*, which can probably be termed as leakage. It is possible that the free SPIO are subjected to endocytosis by macrophages. A similar situation was described in iron oxide-labeled mesenchymal stem cells that were transplanted into a rat model of infarcted myocardium.[16] In addition, iron oxide induces negative contrast in MRI, which, in some cases, can be difficult to attribute to the signal loss of the labeled cells, because of many other sources of negative contrast of MRI in the body.

Our group recently reported the development of a polymeric MRI contrast agent based on a gadolinium-chelated poly(vinyl alcohol).[17] In this study, NIH-3T3 cells were labeled with the contrast agent via electroporation. Cell viability and proliferation were not affected by polymer labeling, and MR measurements showed that labeled cells could be clearly tracked *in vivo*. In this study, we selected EPCs as a stem cell tracking model. The EPCs isolated from the peripheral blood and BM have been used in the therapeutic angiogenesis of ischemic limbs, in stroke, and in myocardial infarction.[18–25]

Advances in the techniques for visualizing EPCs, which are activated by cytokines at the site of injury, are imperative for understanding the mechanisms of proliferation, recruitment, mobilization, and incorporation of EPCs into the foci of vasculogenesis. Although the detection sensitivity of gadolinium chelates is generally lower than that of iron oxide, their positive contrast is easy to detect in a determinant tissue.[26,27] Therefore, we synthesized a water-soluble gadolinium chelate as an alternative MRI contrast agent. This agent, called Dex-DOTA-Gd^{3+}, was designed for labeling EPCs. Dex-DOTA-Gd^{3+} was delivered into EPCs by electroporation to investigate its feasibility for cellular imaging and its capability for tracking the fate of the cells *in vivo* over long periods. In addition, we defined a procedure for properly visualizing labeled EPCs transplanted into a rat model of ischemic limbs.

Materials and Methods

H-NMR measurements

Proton nuclear magnetic resonance (H-NMR) spectra were recorded using a 300-MHz 7.1-T NMR spectrometer (Gemini 2000/300; Varian Inc.). The concentration of paramagnetic species Gd(III) was measured by inductively coupled plasma atomic emission spectroscopy (Model 7510; Shimadzu Co., Kyoto, Japan).

Synthesis of Dex-DOTA-Gd^{3+}

Amination of dextran (MW, 40 kD) was conducted as follows: dextran (10 mmol sugar unit) was dissolved in 60 mL of anhydrous dimethylsulfoxide followed by addition of 1,1′-carbonylbis-1H-imidazole (7.5 mmol). The reaction was allowed to proceed under a nitrogen atmosphere at room temperature for 4 h. 1,3- propanediamine (75 mmol) was then added to the resulting reaction mixture, which was then stirred overnight at room temperature. The reaction product was subsequently purified by dialysis (Spectra/Pore membrane; MW cut-off = 10 kDa) in distilled water. The remaining solution was lyophilized, and dextran-diamine was obtained. About 1% of the total amino groups were reacted with fluorescein-5-EX, succinimidyl ester (FITC; Invitrogen, Molecular Probes®, Eugene).

^{1}H-NMR (D_2O): δ 4.99 (br,CHO_2), 3.605 (br,CHOH), 3.769 (br,CHOH), 5.2 (br,CHO), 3.253 (br,C(=O)$NHCH_2$), 2.88 (br,CH_2NH_2), 1.792 (br,$CH_2CH_2CH_2$), 3.53 (br,CHOH), 3.922–3.983 (br,$CHCH_2$).

Dextran-diamine was diluted in 60 mL of anhydrous dimethylsulfoxide and reacted with mono-N-succinimidyl 1,4,7,10-tetraazacyclododecane-1,4,7,10-tetraacetate (DOTA, 1 mmol of NH_2 in dextran-diamine: 1.2 mmol of DOTA) under a nitrogen atmosphere at room temperature for 1 day. The reaction mixture was purified in distilled water by using a dialysis membrane (Spectra/Pore membrane; MW cut-off = 10 kDa). The final solution was lyophilized, and dextran-diamine-DOTA was obtained.

^{1}H-NMR (D_2O): δ 5.02 (br,CHO_2), 3.63 (br,CHOH), 3.77 (br,CHOH), 5.2 (br,CHO), 3.3 (br,C(=O)CH_2N), 3.51 (br,NCH2C(=O)OH), 3.326 (br,C(=O)$NHCH_2$),br,CH_2CH_2N), 1.91 (br,$CH_2CH_2CH_2$), 3.92 (br,CHOH).

Dextran-diamine-DOTA was diluted in 50 mL of distilled water and treated with 2.2 mole equivalents of gadolinium chloride solution, which was added dropwise with stirring. After the stabilization of the solution with addition of 1 M NaOH to obtain a final pH of 6.6–7.0, the reaction product was stirred for 1 day at room temperature. After this, the reaction mixture was purified in distilled water by using a dialysis membrane (Spectra/Pore membrane; MW cut-off = 10 kDa). The final solution was lyophilized, and dextran-DOTA-Gd^{3+} was obtained (Dex-DOTA-Gd^{3+}).

MRI measurements

T_1-weighted images were obtained in a 1.5-*T* compact MRI system (MRmini; Dainippon Sumitomo Pharma) with a TR of 2000 ms and TE of 9 ms (FOV: 4×8 cm; matrix: 126×256; slice thickness: 1 mm; slice gap: 0 mm; number of slices: 35).

Isolation of EPCs

BM was flushed from the femurs and tibias of F344 rats (4-week-old males) after previous cytokine induced mobilization of BM-derived EPCs by subcutaneous injections of granulocyte colony-stimulating factor (Kirin Pharma) at 200 μg/kg/day over 5 days.[28,29] CD34 and FLK-1 positive BM cells were isolated by magnetic beads (Streptavidin Microbeads; Miltenyi Biotec GmbH) coated with the antibodies CD34 and FLK-1 (sc-6251 and sc-7324; Santa Cruz Biotechnology, Inc.) and by using the biotin labeling kit NH_2 (Dojindo Molecular Technologies, Inc.). Cells were placed in fibronectin-coated dishes and cultured with an endothelial cell basal medium (EBM-2) supplemented with EGM-2 SingleQuots (Clonetics Lonza).[18]

Histological identification of EPCs

One week after isolation, the cells were detached using ReagentPack™ (Clonetics Lonza), and 1×10^5 cells were placed in fibronectin-coated dishes (3.5-mm glass bottom dish; Matsunami Glass IND., Ltd.). Fluorescent staining of adherent cells was used to confirm the EPC phenotype. EPCs were incubated with 1,1′-dioctadecyl-3,3,3′,3′-tetramethylindocarbocyanine perchlorate-labeled acetylated LDL (DiI-acLDL,